The International Journal of Advanced Manufacturing Technology (2018) 98:2849–2863
https://doi.org/10.1007/s00170-018-2483-y

ORIGINAL ARTICLE

A thermo-mechanical coupled model of derivative cutting of microtextured tools

Ran Duan[1] · Jianxin Deng[1] · Dongliang Ge[1] · Xing Ai[1] · Yayun Liu[1] · Rong Meng[1] · Xuemu Li[1] · Hui Chen[1]

Received: 28 March 2018 / Accepted: 17 July 2018 / Published online: 25 July 2018

Abstract
In our previous works, the revelation of the significance of derivative cutting in the cutting process with microtextured tools, which occurs because of the finite sharpness of the texture edge at the tool-chip interface, serves as a starting point for exploring of the cutting mechanism. At present, a thermo-mechanical coupled model for orthogonal cutting process is formulated to predict cutting force under effect of derivative cutting in terms of the structural and positional parameters of textures, cutting conditions, and material properties. The flow stress model considering size effect is combined with the Oxley's cutting model to predict derivative chip formation force. Meanwhile, the Waldorf's slip-line model is applied to evaluate plowing force in derivative cutting. The cutting temperature is predicted based on the heat source theory, which is integrated with the proposed model of derivative cutting to build up the coupled iterative model. A series of orthogonal cutting tests are carried out to validate the prediction model by using different types of microtextured tools. The measured values of cutting force show a good agreement with the predictions. Furthermore, the proposed method provides some insights into ways to diminish the adverse effect of derivative cutting. Results show that the reductions in the edge radius and the inclined angle of textures contribute to decreasing derivative cutting force with increasing cutting velocity.

Keywords Surface texturing · Derivative-cutting · Cutting force

1 Introduction

In recent years, a lot of research work about the textured tools has announced that surface texturing as a mean of improving tribological characteristics at tool-chip interface can perform better cutting performance compared to the conventional cutting tools. The advantages of microtextures for cutting tools are the reducing of contact friction and the keeping of lubrications; hence, it brings about lower cutting forces, cutting temperature, tool wear, and higher surface quality. Currently, considerable efforts have been made to evaluate the effectiveness of microtextures on improving cutting performance in term of the multi-shape and scale parameters, various coatings, and different lubrication conditions by experimental and finite element (FEM) methods. However, the mechanism of cutting process with microtextured tools is not well understood.

Several investigations have focus on the effect of different types of textures on cutting performance of cutting tool, such as dimples, microholes, channels, grooves, and square dots. For example, Xing et al. [1] designed and fabricated three types of textures (linear, circular, and rectangular) on the rake face, the cutting performance of the textured samples have gotten better as compared to conventional tools, and especially, the rectangular textured tool performed best at low cutting speed. Kummel et al. [2] found that BUE held better steady on the dimple textured rake face with respect to linear grooves perpendicular and parallel to the cutting edge and so the dimple textures exhibited fine wear resistance property. Moreover, the cutting performance of textured tools can be further improved by surface coating, filling with solid lubrications, and using cutting fluid. Zhang et al. [3] demonstrated that laser texturing had contribution to improvement of anti-adhesive wear property of WC/Co-based TiAlN coatings via the ball-on-disk wear test and turning experiments. They also reported that microtextures could help the cutting fluid permeate into tool-chip interface, resulting in enhancement of lubrication

✉ Jianxin Deng
jxdeng@sdu.edu.cn

[1] Key Laboratory of High Efficiency and Clean Mechanical Manufacture of MOE, Department of Mechanical Engineering, Shandong University, Jinan 250061, People's Republic of China

condition. It showed that the textures structure could remain and guide the flow of lubrications on the rake face, leading to the steady state of hydrodynamic lift [4]. Deng et al. [5] made microtextures of different geometrical characteristics and filled the solid lubricants (MoS_2) into the microstructure. The cutting tests shown that the ellipse grooved tool got lowest cutting forces, cutting temperature, and the friction coefficient at the tool-chip interface. Moreover, the size level of textures was extended to nanoscale and textured rake faces were deposited with solid lubricant (WS_2) coatings by Deng et al. [6] and found that deposition with nanoscale surface texturing was an effective way to achieve better machinability. Sugihara and Enomoto investigated various types of cutting tools with textured rake and flank faces. The results showed that the structured tools brought about better anti-adhesion property [7, 8] and wear resisitance [9]. Few researchers applied FEM method to assess machining performance of textured tools. For instance, Ma et al. [10] modeled and simulated the orthogonal cutting of mild steel with microbump textured tools and so optimized microbump parameters to minimize the cutting force and faciliate forming process of chip. Han et al. [11, 12] focused on the simulation of phase transformation in the cutting process with textured tools based on a couple Eulerian-Lagrangian (CEL) method. The results showed some of the microgrooves served as microcutters as the chip flows over the rake face, whether in machining of AISI 1045 [11] or Al6061-T6 [12].

Although the advantages of textured tools in the improvement of the cutting performance have been clarified, the unexplained formation mechanism of texture blockage still remains. In our previous research [13], derivative cutting has been demonstrated to be responsible for the blocking phenomenon occurring in textures. Derivative cutting refers to the fact that the chip bottom side is cut by textures on the rake face and the separated material eventually flows into textures. This results in additional power consumption in cutting process and functional failure of textures. Moreover, an analytical model of predicting derivative chip formation has been proposed [14], which has exhibited the forming conditions of the derivative chip. However, the mechanism of derivative cutting is not well understood.

In this work, a thermal-mechanical coupled model is formulated to predict cutting force under the effect of derivative cutting directly from the structural and positional parameters of textures, cutting conditions, and material properties. The flow stress model based on strain gradient plasticity theory is utilized for derivative cutting, which combines with the Oxley's cutting model to predict derivative chip formation force. Meanwhile, Waldorf's slip-line model with flow stress is applied to obtain plowing force in derivative cutting. Cutting temperature is predicted based on heat source theory, which is integrated with the proposed model of derivative cutting to build up the coupled iterative model. In order to verify the proposed model, a series of orthogonal cutting tests are carried out by using different types of microtextured tools.

The framework of the paper includes the following three parts. First, a coupled iteration model according to the moving band heat source theory, slip-line method, and strain gradient plasticity theory is established. Second, an experimental validation of the prediction model is conducted by measuring of cutting forces using the microtextured tools. Finally, an analysis of the proposed model is made to find ways to diminish the adverse effect of derivative cutting.

2 Model development

2.1 Analysis of machining process with derivative cutting

The Oxley's model [15] is introduced to illustrate cutting process under the action of derivative cutting by theoretical analysis method. Figure 1 shows orthogonal machining with derivative cutting. Moreover, Ozel and Zeren [16] have determined that the Johnson-Cook material model [17] can be used in the Oxley's model for the prediction of shear flow stress. According to these well-established models, the machining process with derivative cutting can be modeled as follows.

For given cutting conditions, namely cutting velocity V, cutting depth t_1, and cutting width w, the equivalent strain ε_{AB} and strain rate $\dot{\varepsilon}_{AB}$ in shear plane are

$$\varepsilon_{AB} = \frac{\cos\alpha}{2\sqrt{3}\sin\phi\cos(\phi-\alpha)} \tag{1}$$

$$\dot{\varepsilon}_{AB} = C_0\frac{V_S}{\sqrt{3}l_{AB}} \tag{2}$$

where α is the rake angle, ϕ is the shear angle for the shear plane AB, and C_0 is the material constant, namely the thickness-length ratio at the primary zone. Moreover, the shear velocity V_S and shear plane length l_{AB} are given

$$V_S = \frac{V\cos\alpha}{\cos(\phi-\alpha)} \tag{3}$$

$$l_{AB} = \frac{t_1}{\sin\phi} \tag{4}$$

Combining with Eqs. (1), (2), (3), and (4), the shear stress k_{AB} can be obtained according to Johnson-Cook material model [17] as

$$k_{AB} = \frac{1}{\sqrt{3}}\left(A + B\varepsilon_{AB}^{n}\right)\left[1 + C\ln\left(\frac{\dot{\varepsilon}_{AB}}{\dot{\varepsilon}_0}\right)\right]\left[1-\left(\frac{T_{AB}-T_0}{T_m-T_0}\right)^{m}\right] \tag{5}$$

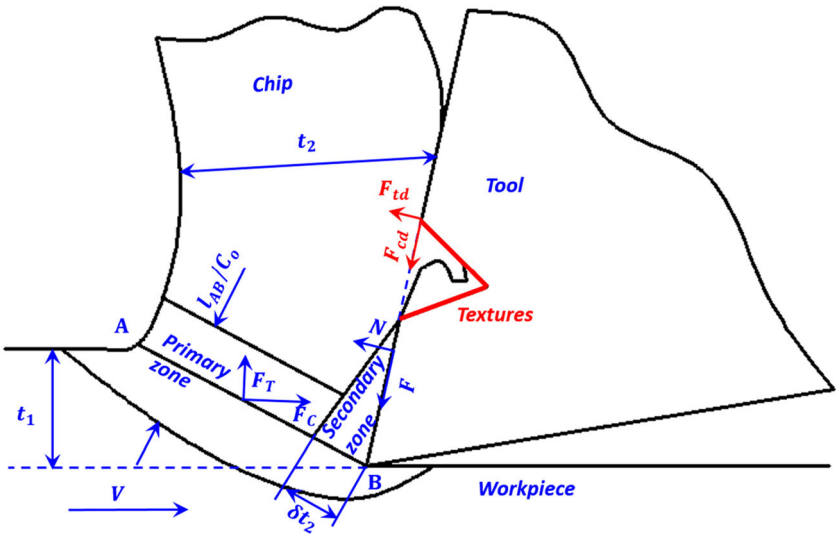

Fig. 1 Orthogonal machining with derivative cutting

The hydrostatic pressures P_A and P_B of points A and B are given in Eqs. (6) and (7).

$$P_A = k_{AB}\left[1 + 2\left(\frac{\pi}{4} - \phi\right)\right] \tag{6}$$

$$P_B = k_{AB}\left\{2\tan\theta - \left[1 + 2\left(\frac{\pi}{4} - \phi\right)\right]\right\} \tag{7}$$

where θ represents the angle of the resultant force of F_C and F_T relative to the shear plane as given in Eq. (8).

$$\theta = \tan^{-1}\left(1 + 2\left(\frac{\pi}{4} - \phi\right) - Cn\right) \tag{8}$$

Considering the material strain in combination with Johnson-Cook material model, the value of the constant Cn can be calculated by Eq. (9).

$$Cn = C_0 n \frac{B\varepsilon_{AB}^n}{A + B\varepsilon_{AB}^n} \tag{9}$$

Based on Li's work [18], the distance between cutting edge B and the action point of the resultant force of F_C and F_T is given

$$X_s = \frac{l_{AB}(2P_A + P_B)}{3(P_A + P_B)} \tag{10}$$

According to Zorev's work [19], the normal stress distribution at the tool-chip interface can be expressed as a power-law function as shown in Eq. (11).

$$\sigma_N(x) = \sigma_{N_{\max}}\left[1 - \left(\frac{x}{l_c}\right)^a\right] \tag{11}$$

where $\sigma_{N_{\max}}$ is shown by [15]

$$\sigma_{N_{\max}} = P_B + 2k_{AB}(\phi - \alpha) \tag{12}$$

In Eqs. (13) and (14), the tool-chip contact length l_c and power exponent a are unknown and can be calculated by solving equations based on the moment and force equilibrium laws. In detail,

$$\int_0^{l_c} w\sigma_{N_{\max}}\left[1 - \left(\frac{x}{l_c}\right)^a\right] x dx + F_{td} l_d = F_T X_s \tag{13}$$

$$\int_0^{l_c} w\sigma_{N_{\max}}\left[1 - \left(\frac{x}{l_c}\right)^a\right] dx + F_{td} = F_C \cos\alpha - F_T \sin\alpha \tag{14}$$

and denting

$$I = \frac{F_C\cos\theta - F_T\sin\theta - F_{td}}{w\sigma_{N_{\max}}}, \quad II = \frac{2(F_N X_S - F_{td} l_d)}{w\sigma_{N_{\max}}}$$

Combining Eqs. (13) and (14), the contact length l_c and the power exponent a can be obtained as

$$a = \frac{I^2}{-(I^2 - II) + \sqrt{II^2 - I^2 II}} \tag{15}$$

$$l_c = \frac{II + \sqrt{II^2 - I^2 II}}{I} \tag{16}$$

According to the power law assumption [19], the tool-chip contact area is assumed to be divided into two distinct regions, namely the sticking region and sliding region. The shear stress remains a fixed value (τ_{int}) in sticking region with the length of l_p. Based on the cutting model [15], the length l_p and the frictional force F can be calculated from Eqs. (17) and (18).

$$l_p = \frac{\delta t_2}{\sin(\phi - \alpha)} \tag{17}$$

$$F = \int_0^{l_p} w\tau_{\text{int}} dx + \frac{w\tau_{\text{int}}}{\sigma_N(l_p)} \int_{l_p}^{l_c} \sigma_N(x) dx \tag{18}$$

The force components on the shear plane and the tool rake face yield the relation in Eq. (19)

$$\int_0^{l_p} w\tau_{\text{int}}dx + \frac{w\tau_{\text{int}}}{\sigma_N(l_p)}\int_{l_p}^{l_c}\sigma_N(x)dx + F_{cd} = F_C\sin\alpha + F_T\cos\alpha \tag{19}$$

Equation (20) leads to the expression for τ_{int} as

$$\tau_{\text{int}} = \frac{F_C\sin\alpha + F_T\cos\alpha - F_{cd}}{wl_p + \frac{w}{\sigma_N(l_p)}\int_{l_p}^{l_c}\sigma_N(x)dx} \tag{20}$$

The average strain and strain rate at secondary deformation zone can be obtained by [15]

$$\varepsilon_{\text{int}} = \frac{l_p}{\sqrt{3}\delta t_2} \tag{21}$$

$$\dot{\varepsilon}_{\text{int}} = \frac{V_c}{\delta t_2} \tag{22}$$

So, the tool-chip flow stress k_{chip} can be obtained as

$$k_{\text{chip}} = \frac{1}{\sqrt{3}}[A + B(\varepsilon_{\text{int}})^n]\left[1 + C\ln\left(\frac{\dot{\varepsilon}_{\text{int}}}{\dot{\varepsilon}_0}\right)\right]\left[1 - \left(\frac{T_{\text{int}} - T_0}{T_m - T_0}\right)^m\right] \tag{23}$$

2.2 Modeling of temperature distribution in cutting zones

The temperature distribution for cutting process with the textured tools needs to be analytically represented since it not only affects the cutting forces and tool wear but also is used to determine derivative cutting force. Based on the Jaeger's heat source method [20], Hahn [21] build up an analytical model of temperature in cutting process. Figure 2 shows that the moving band heat source of an angle φ with the direction of velocity can be represented as the oblique red line, and so the temperature rise at a point H (x, z) can be formulated as

$$T_H(X,Z) = \frac{q}{2\pi\lambda}\int_{l_i=0}^{L} e^{-(X - l_i\sin\varphi)(v/2a_i)} K_0\left[\frac{v}{2a_i}\sqrt{(X - l_i\sin\varphi)^2 + (Z - l_i\cos\varphi)^2}\right]dl_i \tag{24}$$

where λ and a are the thermal conductivity and thermal diffusivity of the medium, respectively; $X - l_i\sin\varphi$ is the projection of the distance $\sqrt{(X - l_i\sin\varphi)^2 + (Z - l_i\cos\varphi)^2}$ between dl_i and the point H in the direction of the velocity v. K_0 denotes a zero order Bessel function of the second kind. In addition, the thermal diffusivity a can be formulated as

$$a = \frac{\lambda}{\rho c_p} \tag{25}$$

where ρ is material density, and C_p is specific heat.

From Komanduri and Hou's [22] work seen in Fig. 3, the thermal rise at a point M (x, z) for the shear plane can be evaluated by using Eq. (26)

$$T_{\text{chip}}^{\text{shear}}(X,Z) = \frac{q_{\text{shear}}}{2\pi\lambda_{\text{chip}}}\int_0^{l_{AB}} e^{-\frac{(X - x_i)V_c}{2a_{\text{chip}}}} \left\{ \begin{array}{l} K_0\left(\frac{V_c}{2a_{\text{chip}}}\sqrt{(X - x_i)^2 + (Z - z_i)^2}\right) + \frac{1}{2}K_0\left(\frac{V_c}{2a_{\text{chip}}}\sqrt{(X - x_i)^2 + (2t_1 - Z - z_i)^2}\right) \\ + \frac{1}{2}K_0\left(\frac{V_c}{2a_{\text{chip}}}\sqrt{(X - x_i)^2 + (Z + z_i)^2}\right) \end{array} \right\} dl_i \tag{26}$$

where $x_i = l - l_i\sin(\phi - \alpha)$, $z_i = l_i\cos(\phi - \alpha)$, and $l_{AB} = t_1/\cos(\phi - \alpha)$. Moreover, the heat intensity q_{shear} of shear plane can be formulated as

$$q_{\text{shear}} = \frac{F_s V_s}{l_{AB} w}$$

The next step is to model the thermal rise under the effect of nonuniform heat intensity by considering friction at tool-chip interface and derivative cutting. Although the difference of shear stress between the sticking and sliding zone of tool-chip interface makes the nonuniform heat generation rate of the friction heat source, Huang and Liang [23] converted uniform shear stress to the shear stress distribution by using recommended values from other studies. In addition, the influence of derivative cutting needs to be considered; the equivalent shear stress τ_s can be obtained by using Eq. (27).

$$\tau_s = \frac{F + F_{cd}}{w(l_p + 0.5l_s)} \tag{27}$$

where l_p represents the sticking contact length, l_s represents the sliding contact length, w represents the width of chip, F represents the friction force, and F_{cd} represents the derivative cutting force along tool-chip interface. The heat intensity q_{int} keeps constant as $\tau_s V_c$ along sticking zone and linearly decreases from $\tau_s V_c$ to zero, which is used for thermal modeling along the interface. From Huang and

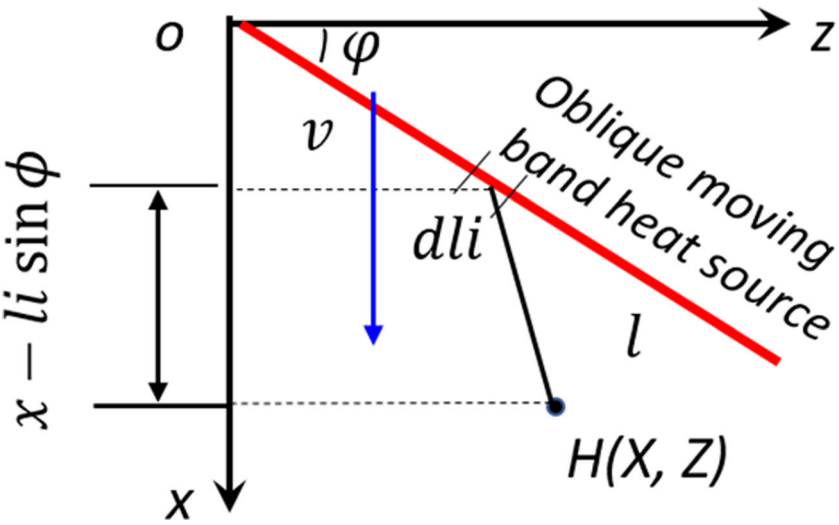

Fig. 2 The diagram of the moving band heat source method

Liang's [23] work, the thermal rise at a point M (x, z) in the chip as shown in Fig. 4 can be obtained as

$$T_{\text{chip}}^{\text{int}} = \frac{1}{\pi\lambda_{\text{chip}}}\int_0^{l_c} B(x)q_{\text{int}}(x)e^{-\frac{(X-x)V_c}{2a}} \left[K_0\left(\frac{R_iV_c}{2a_{\text{chip}}}\right) + K_0\left(\frac{R_i'V_c}{2a_{\text{chip}}}\right) + K_0\left(\frac{R_i''V_c}{2a_{\text{chip}}}\right)\right]dx \tag{28}$$

where $B(x)$ is heat partition fraction, $R_i = \sqrt{(X-x)^2 + Z^2}$, $R_i' = \sqrt{(X-x)^2 + (2t_2-Z)^2}$, and $R_i'' = \sqrt{(X-x)^2 + (2t_2+Z)^2}$.

Since the tool-chip heat source is stationary to the tool, it is assumed that the heat $[1-B(x)]q_{\text{friction}}$ is transmitted into the tool. Meanwhile, the flank face is treated as an adiabatic boundary. The thermal rise at any point M (X′, Y′, Z′) in the tool side is shown as

$$T_{\text{tool}}^{\text{int}}\left(X', Y', Z'\right) = \frac{1}{2\pi\lambda_{\text{tool}}}\int_0^{l_c}[1-B(x)]q_{\text{int}}\left(x'\right)dx'\int_{-\frac{w}{2}}^{\frac{w}{2}}\left(\frac{1}{R_i} + \frac{1}{R_i'}\right)dy' \tag{29}$$

where $R_i = \sqrt{(X'-x')^2 + (Y'-y')^2 + Z'^2}$ and $R_i' = \sqrt{(X'-2l_c+x')^2 + (Y'-y')^2 + Z'^2}$.

To find the fraction $B(x)$, the tool-chip heat source is dispersed into n segments. The heat partition ratio B_i corresponding to each segment can be considered as a fixed value. Since the thermal rises of the two sides at the tool-chip interface should be the same, that is

$$T_{\text{chip}}^{\text{shear}}(X,0) + T_{\text{chip}}^{\text{friction}}(X,0) + T_0 = T_{\text{tool}}^{\text{friction}}\left(X', 0, 0\right) + T_0 \tag{30}$$

Considering the distribution discretization of heat partition ratio, Eq. (30) can be transformed by using the matrixing method as follows:

$$[A_1]_{n\times n}[B]_{n\times 1} = [A_2]_{n\times 1} \tag{31}$$

where the elements of matrices can be obtained as

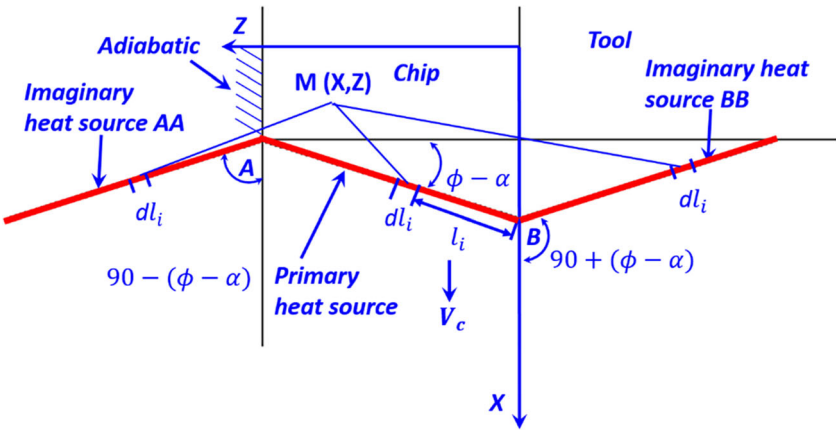

Fig. 3 Schematic of the shear heat sources

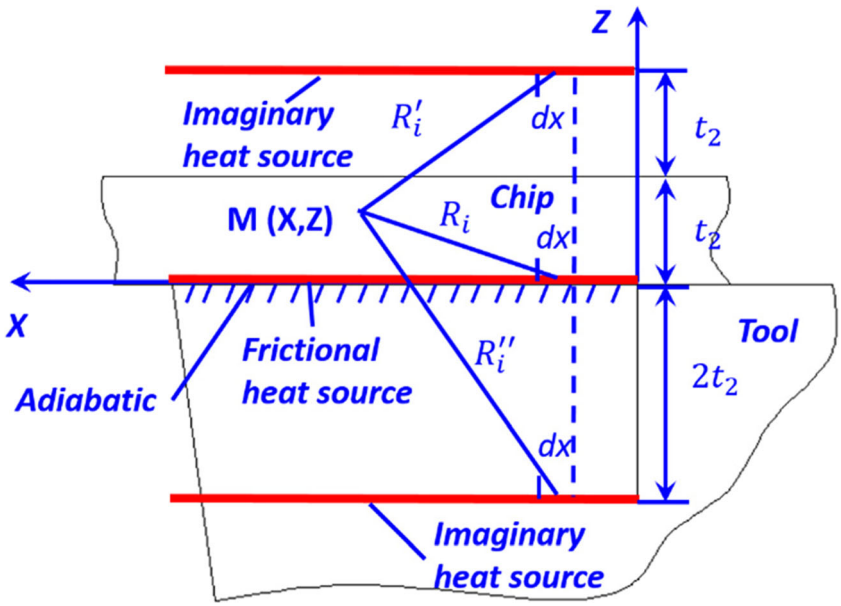

Fig. 4 Schematic of tool-chip heat sources

$$[A_1]_{n\times n}(i,j)=\frac{1}{2\pi\lambda_{\text{tool}}}q_{\text{int}}\left(x_j^{'}\right)\int_{-\frac{w}{2}}^{\frac{w}{2}}\left(\frac{1}{\sqrt{\left(x_i^{'}-x_j^{'}\right)^2+y'^2}}+\frac{1}{\sqrt{\left(x_i^{'}-2l_c+x_j^{'}\right)^2+y'^2}}\right)dy^{'}$$
$$+\frac{1}{\pi\lambda_{\text{chip}}}q_{\text{int}}(x_j)e^{-\frac{(x_i-x_j)V_c}{2a_{\text{chip}}}}\left\{K_0\left(\frac{\sqrt{(x_i-x_j)^2}V_c}{2a_{\text{chip}}}\right)+2K_0\left(\frac{\sqrt{(x_i-x_j)^2+4t_2^2}V_c}{2a_{\text{chip}}}\right)\right\}$$

$$[A_2]_{n\times 1}(i)=\frac{1}{2\pi\lambda_{\text{tool}}}\int_0^{l_c}q_{\text{int}}\left(x^{'}\right)dx^{'}\int_{-\frac{w}{2}}^{\frac{w}{2}}\left(\frac{1}{\sqrt{\left(x_i^{'}-x_j^{'}\right)^2+y'^2}}+\frac{1}{\sqrt{(x_i^{'}-2l_c+x^{'})+y'^2}}\right)dy^{'}$$
$$-\frac{q_{\text{shear}}}{4\pi\lambda_{\text{chip}}}\int_0^{l_{AB}}e^{-\frac{(x_i-X_i)V_c}{2a_{\text{chip}}}}\left\{K_0\left(\frac{V_c}{2a_{\text{chip}}}\sqrt{(x_i-X_i)^2+(2t_2-Z_i)^2}\right)+3K_0\left(\frac{V_c}{2a_{\text{chip}}}\sqrt{(x_i-X_i)^2+Z_i^2}\right)\right\}dl_i$$

The distribution of $B(x)$ can be obtained from the discrete value of B_i by solving Eq. (31). Therefore, the temperature distribution at tool-chip interface can be expressed as

$$T(x)=T_{\text{chip}}^{\text{shear}}(X,0)+T_{\text{chip}}^{\text{int}}(X,0)+T_0 \tag{32}$$

2.3 Analysis modeling of derivative cutting

Firstly, the uncut derivative chip thickness needs to be determined under a given cutting condition. Since the microgroove results in the finite contact length l_d less than the nature contact length, the chip will flow into the groove, forming the inflow angle η of chip bottom side. Figure 5 shows that inflow angle η depends on the rake angle α and the chip stream angle η_b. Therefore, the inflow angle can be obtained by Eq. (33).

$$\eta=\eta_b-\alpha \tag{33}$$

The chip stream angle as an important parameter for the analysis of restricted contact machining has been analyzed by using various slip-line models. For the value of l_d/t_1 (seen in Fig. 5) less than 1.0, the chip stream angle in derivative cutting is made available from the established slip-line models with neglect of chip up-curl radius for machining with restricted contact tools [24]. There are two assumptions [25], that is (1) the influences of strains, strain rates, and temperature on the material flow stress are not taken into account, and (2) slip-line modeling of

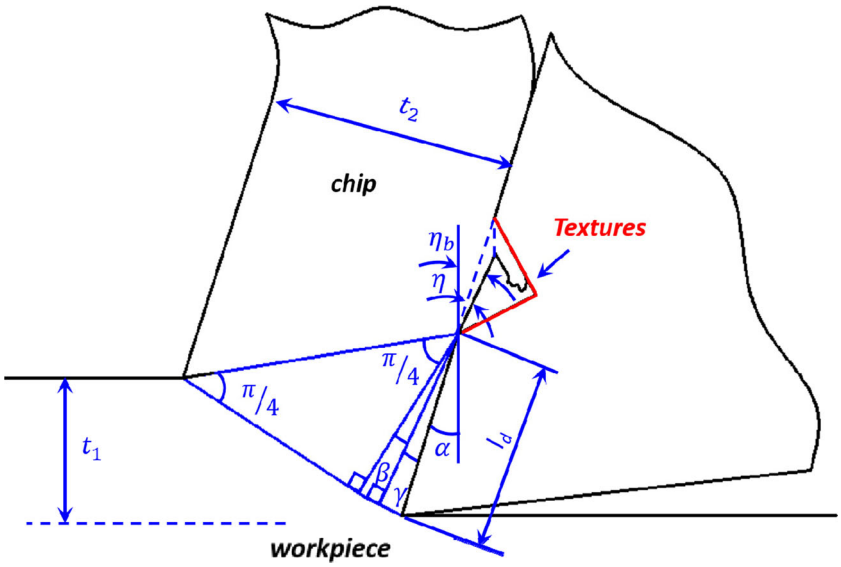

Fig. 5 Simplified deformation zone of chip bottom side

orthogonal cutting is based on the plane strain deformation assumption. At the same time, cutting edge radius needs to be ignored. From the standpoint of restricted contact machining modeling, Johnson [22] and Usui and Hoshi [26] have established the effective theoretical basis. The centered fan slip-line field from these studies is used for analysis of uncut derivative cutting thickness as shown in Fig. 5. The chip stream angle η_b can be obtained from Jawahir's investigation [27] by using Eq. (34).

$$\eta_b = \tan^{-1}\left\{\frac{\cos\gamma}{\cos\alpha\sin(\gamma+\alpha+\beta)} - \cot(\gamma+\alpha+\beta)\right\} \quad (34)$$

where α is the rake angle of the cutting tool, and β and γ represent the two slip-line angles as shown in Fig. 6. Moreover, the silp-line angles β and γ can be obtained by

$$\beta = \cos^{-1}\left[\frac{\cos\alpha - t_1/h}{\sqrt{2}\cos\gamma}\right] - (\pi/4 + \gamma + \alpha) \quad (35)$$

$$\gamma = {}^{1}/_{2}\cos^{-1}(\tau/k) \quad (36)$$

where τ is the frictional stress at tool-chip interface and k is the material flow stress. Equation (36) shows that for a given cutting condition the γ depends on the friction parameter τ/k. The ratio τ/k can quantitatively feature the tool-chip friction state. Fang and Jawahir [24] have pointed out that the relationship of cutting condition and the ratio τ/k for machining with the restricted contact tools. Since the distance between the textures and cutting edge is always designed to be slightly larger than uncut chip thickness, namely t_1/l_d close to 1.0, and tool rake angle is not negative, the ratio value τ/k of 1.0 is considered reasonable.

In addition, the elastic springback of the chip bottom side also needs to be considered. When chip flow over the microgroove of textures, the chip bottom side turns to the free surface, leading to releasing the stored elastic strain energy. According to the general Hook's law [28], the recovery angle η_e can be obtained by

$$\eta_e = \frac{\tau}{G} \quad (37)$$

where G is shear modulus. The effect of temperature on the property of workpiece material needs to be taken into account in the machining process. The shear modulus G derived from the temperature-dependent elastic material parameters (Young's modulus E and Poisson ratio ν) [29] is as follows:

$$\begin{cases} E(T) = E + e_1(T) + e_2(T)^2 \\ \nu(T) = \nu + \Delta\nu(T) \\ G(T) = \dfrac{E(T)}{2(1+\nu(T))} \end{cases} \quad (38)$$

where the e_1, e_2, and $\Delta\nu$ are material parameters. Considering the additional factor of the recovery angle η_e, the chip inflow angle can be modified as

$$\eta = \eta_b + \eta_e - \alpha \quad (39)$$

The uncut derivative chip thickness t_d for the microgroove width w_d is expressed by Eq. (40).

$$t_d = w_d\sin^2\eta \quad (40)$$

The reduction in the scale of deformation results in an increase of strain gradient even the total stain is relatively low [30]. The asymmetric stress distribution in a direction parallel and perpendicular to the shear plane generates inhomogeneous strain gradients, resulting in intensifying of

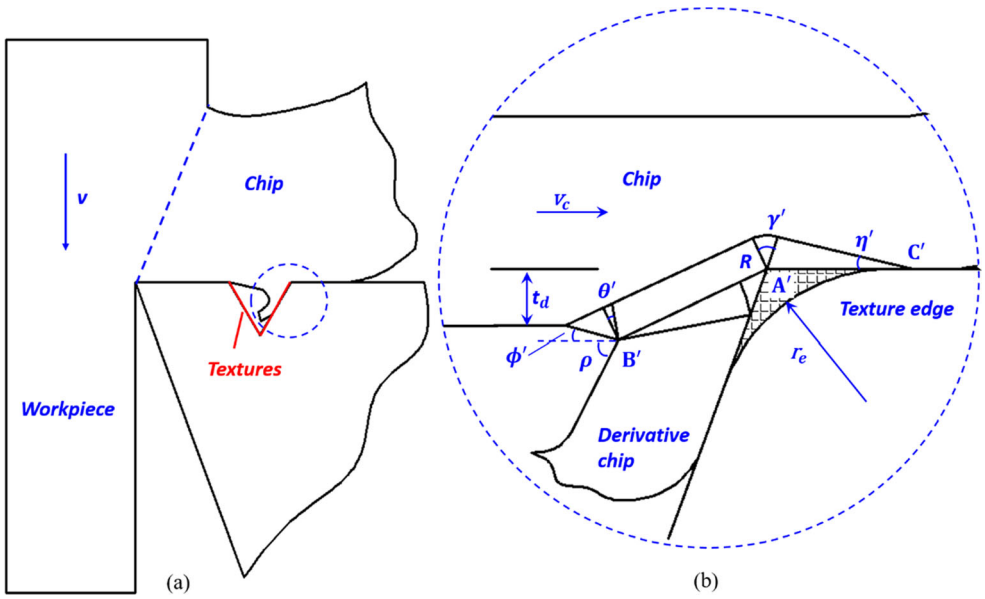

Fig. 6 **a** The diagram of machining with the derivative cutting. **b** The slip-line model for plowing in the derivative cutting process

the size effect. In our previous work [13], the scale of cutting depth in derivative cutting has been demonstrated to belong to microlevel. Unlike the constitutive equations of workpiece material for macrocutting as a function of the strain, strain rate, and temperature, the constitutive equations in the derivative cutting process need to be modified based on the strain gradient theory. The material flow stress in derivative cutting resulting from Joshi and Melkote's work [30] can be calculated by

$$\tau = \tau_{\text{ref}} \sqrt{1 + \frac{2\alpha_c{}^2 G^2 b \sin\left(\phi'\right)}{t_d \tau_{\text{ref}}^2}} \tag{41}$$

where α_c is the stress parameter, G is the shear modulus, b is the magnitude of the Burgers vector, and ϕ' is the shear angle of derivative cutting. Moreover, the Johnson-Cook material model can be chosen as the reference flow stress (τ_{ref}), and then the Eq. (41) is changed as Eq. (42).

$$\tau = \tau_{JC} \sqrt{1 + \frac{2\alpha_c{}^2 G^2 b \sin\left(\phi'\right)}{t_d \tau_{JC}^2}} \tag{42}$$

Since the uncut derivative chip thickness is of the order of the textures edge radius, not only chip formation forces but also plowing forces need to be considered at the same time. The plowing process of derivative cutting is complex. As such, modeling of plowing process has attracted great attention of researchers, and the most significant contribution to the field is the analytical model proposed by Waldorf et al. [31] to predict plowing forces based on the slip-line method. Moreover, it is assumed that built-up edge is stably adhered to the texture edge in the Waldorf's model, and this phenomenon also commonly exists in our previous work about derivative cutting [13]. The plowing with the texture edge of radius r_e is showed in Fig. 6. The shade zone represents the built-up edge and point A′ is the separation point of material. A′B′ is the traditional shear plane with the shear angle ϕ'. Therefore, the plowing forces in the cutting and thrust direction respectively are P_{cut} and P_{thrust}, and these forces are obtained as

$$P_{\text{cut}} = \tau w \left[\cos\left(2\eta'\right)\cos\left(\phi' - \gamma' + \eta'\right) + \left(1 + 2\theta' + 2\gamma' + \sin\left(2\eta'\right)\right) \sin\left(\phi' - \gamma' + \eta'\right)\right] \cdot C'A' \tag{43}$$

$$P_{\text{thrust}} = \tau w \left[\left(1 + 2\theta' + 2\gamma' + \sin\left(2\eta'\right)\right)\cos\left(\phi' - \gamma' + \eta'\right) - \cos\left(2\eta'\right) \sin\left(\phi' - \gamma' + \eta'\right)\right] \cdot C'A' \tag{44}$$

where the related parameters are obtained as follows:

$$\theta' = \frac{\pi}{4} - \rho - \phi'$$

$$\gamma' = \eta' + \phi' - \sin^{-1}\left(\sqrt{2}\sin(\rho)\sin\left(\eta'\right)\right)$$

$$C'A' = \frac{R}{\sin\eta'}$$

$$\gamma' = \eta' + \phi' - \sin^{-1}\left(\sqrt{2}\sin(\rho)\sin\left(\eta'\right)\right)$$

$$R = \sin\left(\eta'\right)\sqrt{\left[r_e \tan\left(\frac{\pi}{4} + \frac{\alpha'}{2}\right)^2 + \frac{\sqrt{2}R\sin(\rho)}{\tan\left(\frac{\pi}{2} + \alpha'\right)}\right]^2 + 2[R\sin(\rho)]^2}$$

As above discussion, the derivative cutting forces are the combination of the formation forces of derivative chip

($F_c^{'}$, $F_t^{'}$) and plowing forces (P_{cut}, P_{thrust}), which are obtained by Eq. (45).

$$\begin{cases} F_{cd} = F_c^{'} + \mathrm{P}_{\text{cut}} \\ F_{td} = F_t^{'} + P_{\text{thrust}} \end{cases} \tag{45}$$

3 Solution of the model

The object of this section is to build up a numerical iterative algorithm for the prediction of cutting force in the machining process with the derivative cutting. Figure 7 shows the general scheme of the thermo-mechanical coupled model. The cutting conditions including cutting parameters, tool geometry, and workpiece properties are closely relevant to the derivative cutting. At the same time, the derivative cutting has influence on the stress state and temperature distribution in machining with microtextured tools.

At the beginning of the iterative computations, the effect of derivative cutting is not considered. According to Oxley's prediction model, the cutting parameters containing cutting velocity v, cutting width w, and feed rate f, took geometry (rake angle α), and physical parameters of workpiece material conduct as inputs. The flowchart of the Oxley's prediction model is shown in Fig. 8. Obviously, it is showed that the values of the initial parameters, including the shear angle ϕ, strain rate constant δ, and material constant C_0, are determined based on the constraint bounds. The program of the iterative algorithm can be run based on these initial variables.

The initial flow stress k_{AB} and chip velocity V_c obtained from the previous step are used to calculate the initial thermal rise $T_{\text{chip}}^{\text{shear}}(X, Z)$ in Eq. (26). The initial average temperature in shear plane is obtained by Eq. (46)

$$T_{AB} = \frac{\int_0^{l_{AB}} T_{\text{chip}}^{\text{shear}}(X, Z) dl_i}{l_{AB}} + T_0 \tag{46}$$

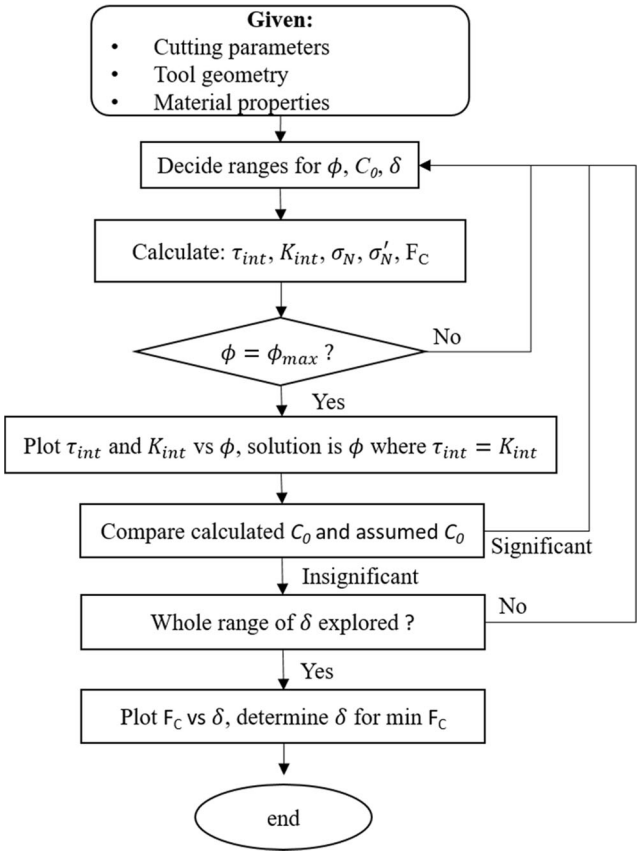

Fig. 8 Flowchart of the Oxley's prediction model

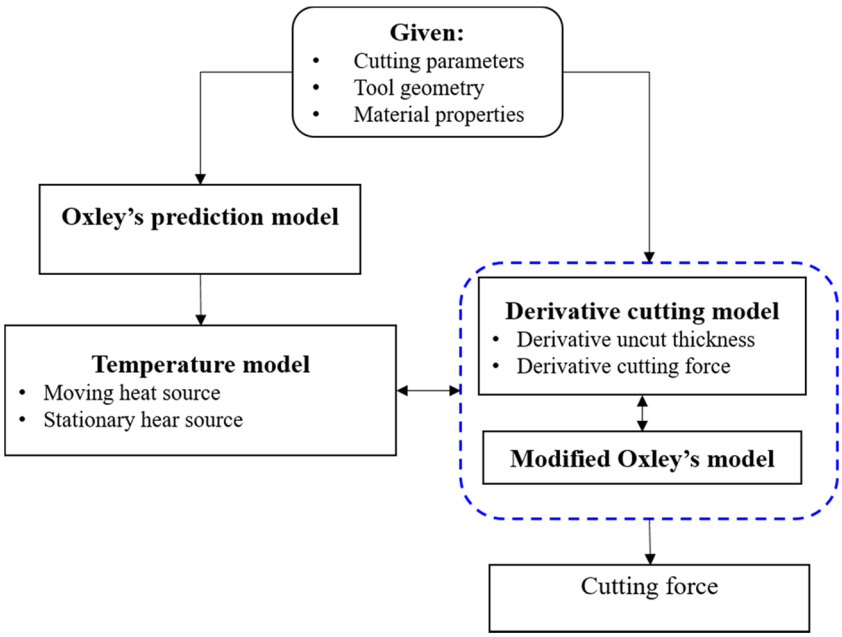

Fig. 7 General scheme of the thermo-mechanical coupled model

Moreover, once $B(x)$ is determined according to Eq. (30), the initial average temperature in the tool-chip contacting zone is calculated by Eq. (47).

$$T_{\text{int}} = \frac{\int_0^{l_c} \left(T_{\text{chip}}^{\text{shear}}(X,0) + T_{\text{chip}}^{\text{int}}(X,0) \right) dl_i}{l_c} + T_0 \tag{47}$$

Meanwhile, the temperature in the position where the chip begins to flow into the textures should be predicted as the initial temperature T_{0d} for the calculation of the flow stress in derivative cutting as shown in Eq. (41). The temperature T_{0d} can be obtained as follows:

$$T_{0d} = T_{\text{chip}}^{\text{shear}}(l_d, 0) + T_{\text{chip}}^{\text{friction}}(l_d, 0) + T_0 \tag{48}$$

The uncut derivative chip thickness is predicted depending on the slip-line theory and elastic property of material as shown in Eq. (39). The derivative cutting velocity actually is the chip velocity. Based on Oxley' prediction model combining with the flow stress model for derivative cutting, the formation force of derivative chip can be predicated, in which the flow stress and shear angle are also obtained. The obtained flow stress and shear angle are used to calculate the plowing force considering the radius of texture edge based on the Waldorf's model. The derivative cutting force is the sum between the formation force of derivative chip and plowing force. The flowchart of calculating the derivative cutting force is seen in Fig. 9. Furthermore, the derivative cutting force is used for computation of the correlation variables in machining with derivative cutting (seen in section 2.1).

Finally, the numerical calculation of cutting force is conducted by coupling and iterating the models. The initial variables obtained from the above steps are taken as inputs, and then the iterative computing of cutting force is executed and is terminated until the deviation satisfies the constraint conditions (seen in Fig. 10). Accordingly, under the given cutting conditions, the cutting force can be finally determined.

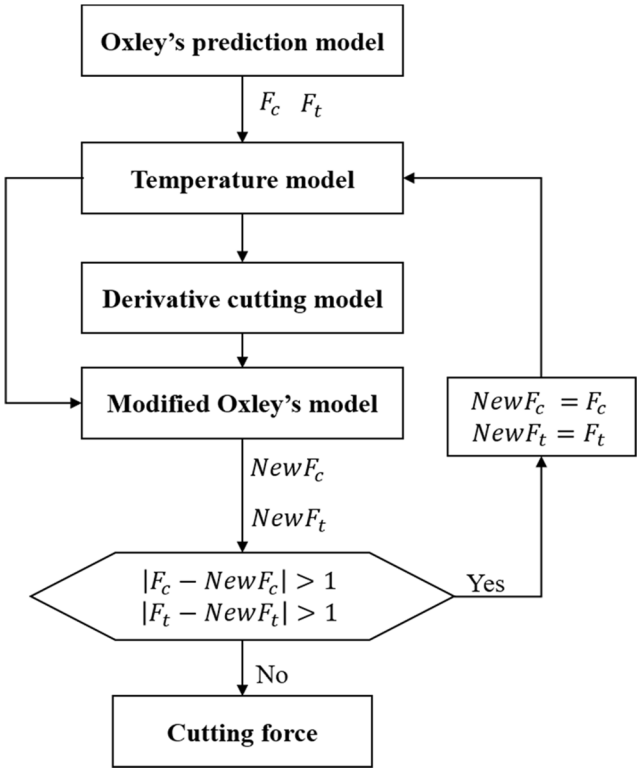

Fig. 10 Flowchart of the numerical calculation of cutting force

4 Experimental setup

Nd/YAG solid-state nanosecond laser is used to fabricate the textures on the rake face of the cutting tools (Type: NG 3189 K420, Kennametal Inc., USA). Table 1 shows some physical parameters of the cutting tools. The type of textures is designed as a single line with the direction of textures parallel to the cutting edge as shown in Fig. 11. The distance l_d between cutting edge and the microgroove increases from 150 to 300 μm at an interval of 50 μm. The three-dimensional structure of the microgroove is measured by the super depth of field microscope (VHX-5000, KEYENCE Co., Ltd., Japan) as shown in Fig. 12c, d. After examined five times, the average

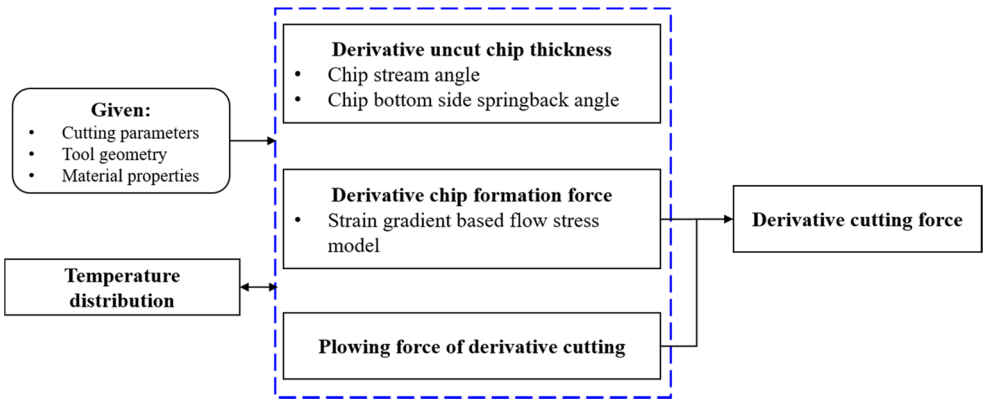

Fig. 9 Flowchart of computation of derivative cutting force

Table 1 Material parameters for the insert

Parameter	E (GPa)	ν	ρ (kg/m^3)	λ (W/m°C)	C_p [J/(kg/°C)]
Value	705	0.23	15,290	46	203

values of the BE edge radius and inclined angle α' are about 5 μm and − 40°, respectively.

A CA6140 lathe is used to conduct orthogonal cutting experiments with the series of textured tools. The textured tools are mounted on the tool holder (2525M3, Kennametal Inc., USA) and the tool rake angle is 0°. The cutting velocities are chosen as 100 and 180 m/min respectively, and feed is selected as 0.1 mm/rev. Due to the difficulty in separating the derivative cutting forces from the other effects, the verification of the model is conducted by comparing the measured and predicted cutting

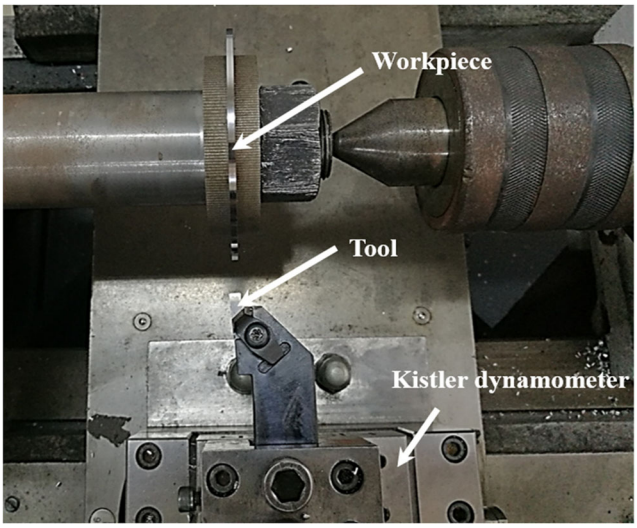

Fig. 12 The experimental setup of orthogonal machining

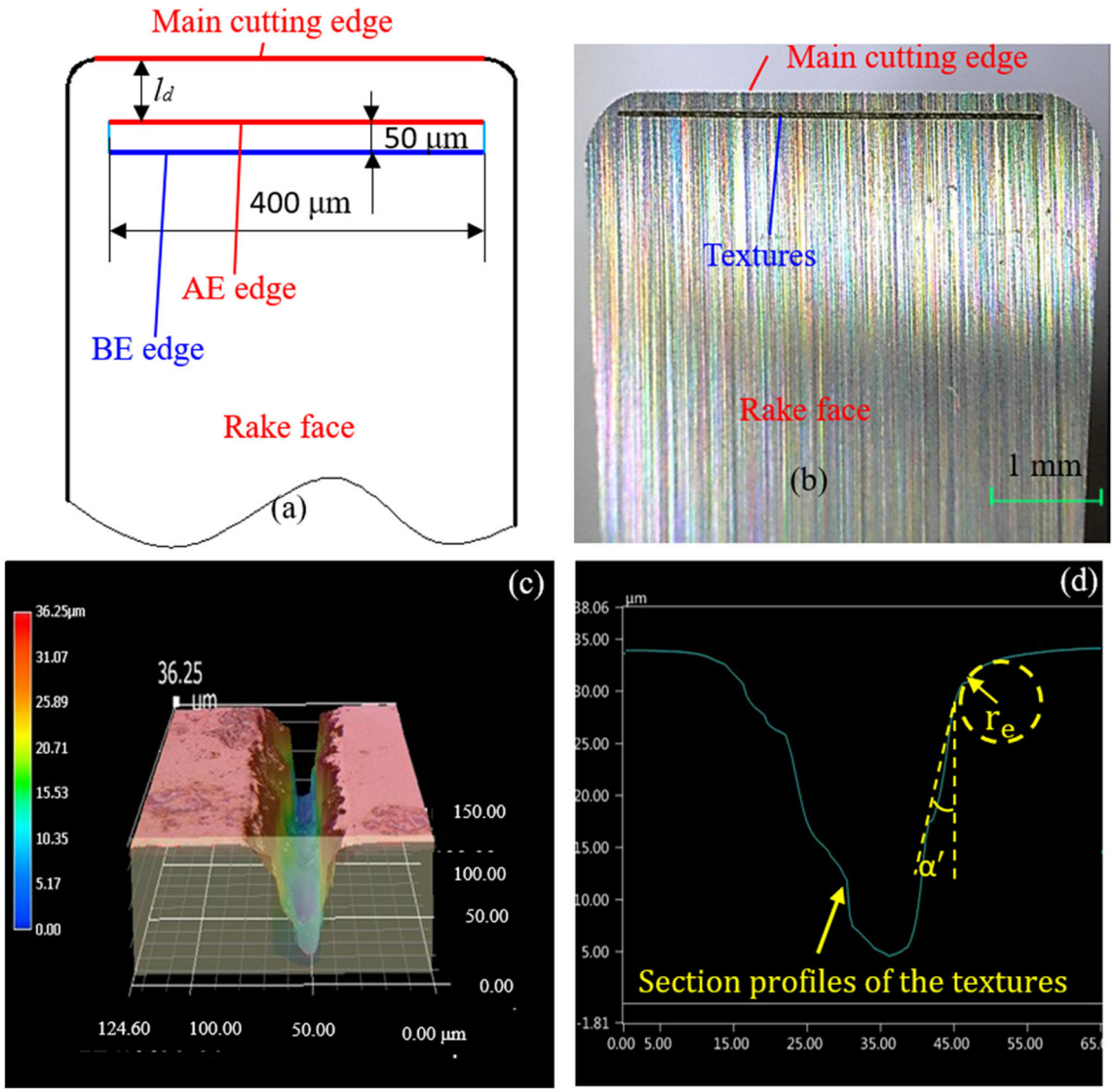

Fig. 11 A microscale textured tool. **a** Schematic of the rake face of textured tool. **b** Photograph corresponding to the textured tool. **c** Width measurement of confocal image of the textures. **d** The related cross section shape

Table 2 Material properties for AISI 1045 [29]

Parameter	AISI 1045	Parameter	AISI 1045	Parameter	AISI 1045
A (MPa)	553	m	1	ν	0.283
B (MPa)	600	$\dot{\varepsilon_0}$ (s^{-1})	1	α_c (KJ/m^2)	50
C	0.0134	e_1 (MPa °C^{-1})	− 52	b (nm)	0.304
n	0.234	e_2 (MPa °C^{-1})	-4.7×10^{-2}	λ (W/m°C)	48
T_0 (°C)	20	$\Delta\upsilon$ (°C^{-1})	4×10^{-5}	ρ (kg/m^3)	7890
T_m (°C)	1460	E (MPa)	2.15×10^5	C_p [J/(kg/°C)]	450

forces. A force sensor (9129AA, Kistler Inc., Swiss) is used to measure the cutting forces. Figure 12 shows the related experimental setup. The workpiece material is AISI 1045 and is pre-prepared in the form of a disk with diameter of 100 mm and thickness of 2 mm. The properties of workpiece material are listed in Table 2.

5 Results and discussions

5.1 Model validation

Figure 13 shows the textures wear morphology for the cutting velocity of 100 m/min. It is observed that all microgrooves of textures are blocked up by derivative chip. It is indicated that derivative cutting took place in the cutting experiments. Similarly, the derivative cutting was found to exist in the cutting experiments for the cutting velocity of 180 m/s. The cutting forces from the experiment measurement and the analytical model are shown in Table 3. The errors are calculated by using the Eq. (49) and listed in Table 3. It is found that the prediction errors of F_C and F_T are respectively from 12.8 to 16.4% and from 1.5 to 11.3%. The predicted cutting forces are found in close agreement with the experimental results, indicating the success of the proposed model.

$$\text{Error} = \frac{|\text{experimental value} - \text{simultated value}|}{\text{experimental value}} \times 100\% \quad (49)$$

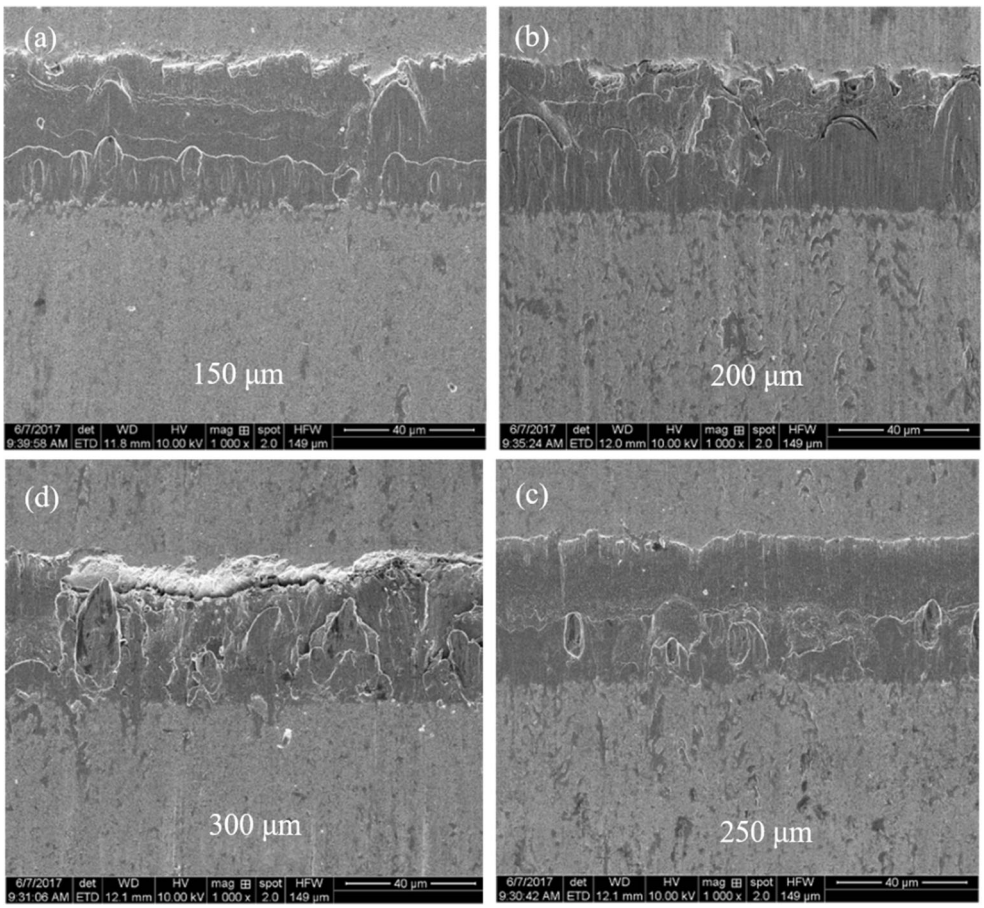

Fig. 13 Wear states of textures with the different distance l_d

Table 3 Comparison between measured and predicted values for cutting force

			Measured		Predicted		Error	
Test	l_d (μm)	V (m/min)	F_C (N)	F_T (N)	F_C (N)	F_T (N)	F_C (%)	F_T (%)
1	150	100	775.6	385.1	676.4	428.8	12.8	11.3
2	200	100	763.4	380.2	653.1	400.4	14.4	5.3
3	250	100	742.8	358.5	622.9	363.9	16.1	1.5
4	300	100	710.3	350.7	593.6	333.5	16.4	4.9
5	150	180	722.3	370.9	639.6	402.8	11.4	8.6
6	200	180	698.1	340.8	614.8	371.9	11.9	9.1
7	250	180	651.0	338.2	602.3	345.5	7.5	2.1
8	300	180	648.9	321.7	587.7	301.9	9.4	6.2

5.2 Influence of the edge radius and inclined angle of the textures on derivative cutting force

Figure 14 presents the relation of the texture edge radius and derivative cutting forces at the cutting velocity of 100 m/min, cutting depth of 0.1 mm, and distance l_d of 150 μm. It is showed that the derivative cutting forces increase with an increase of the texture edge radius r_e. Due to the assumption that a stable build-up is attached to the finite edge radius (seen in Fig. 7), the build-up region C′A′ determines friction stress between uncut chip bottom side and the texture edge. The higher finite radius causes the larger build-up region, resulting in increasing of the friction force. In addition, the Oxley's prediction model in conjunction with the flow stress model based on strain gradient theory is used to estimate derivative chip formation force. The inclined angle of texture is the rake angle in the derivative cutting. According to the cutting theory, it is known that the plastic deformation of chip bottom side increases as the inclined angle of texture becomes more negative, resulting in increasing of derivative cutting forces as shown in Fig. 15.

5.3 Influence of cutting velocity on derivative cutting

Figure 16 shows that derivative cutting forces decreases with increasing of cutting velocity under the conditions of the textures edge radius of 5 μm, the distance l_d of 150 μm, and the inclined angle of − 40°. The influence of cutting velocity on derivative cutting attributes to two aspects. Firstly, derivative cutting force is affected by temperature distribution at tool-chip interface. It has been known that cutting temperature increases with an increase of cutting velocity, leading to increasing thermal softening effect of chip bottom side. Secondly, the flow stress for derivative cutting is modeled by considering size effect. According to Eleiche and Campbell' s study [32], the flow stress is sensitive to the size effect of material in a low cutting velocity range and mainly influenced by the stain rate at high cutting velocity. Meanwhile, strain and strain rate increase with cutting velocity [33], resulting in the aggravation of strain harden. Based on above discussions, Fig. 16 indicates the thermal softening effect is dominant

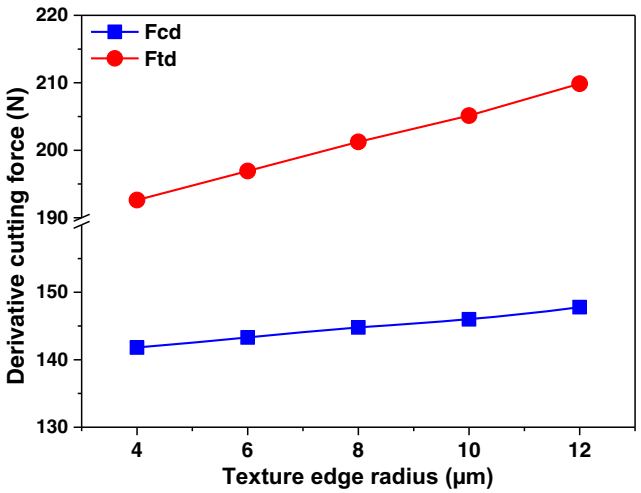

Fig. 14 The effect of the texture edge radius on the derivative cutting forces at the cutting velocity of 100 m/min, cutting depth of 0.1 mm, and distance l_d of 150 μm

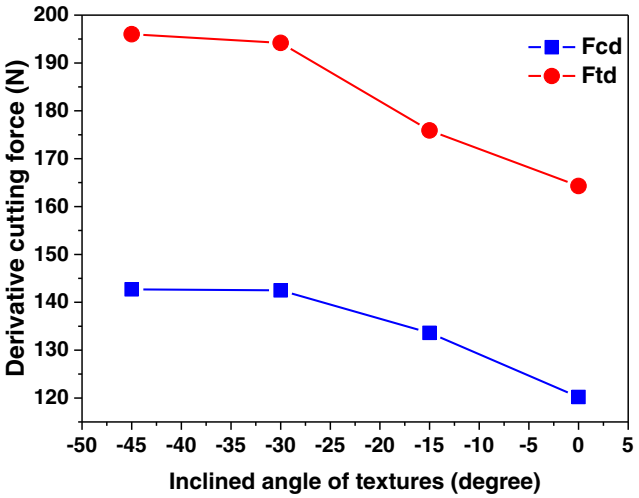

Fig. 15 The effect of the inclined angle of textures on the derivative cutting at the cutting velocity of 100 m/min, cutting depth of 0.1 mm, and distance l_d of 150 μm

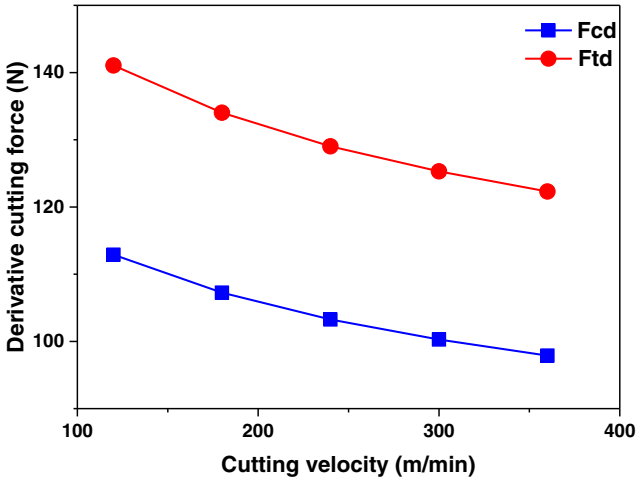

Fig. 16 The effect of cutting velocity on derivative cutting under the constant conditions of the textures edge radius of 5 μm, the distance l_d of 150 μm, and the inclined angle of − 40°

for the reduction of the derivative cutting force with an increase of cutting velocity. Figure 17 shows the comparisons of the predicted cutting force F_c and thrust force F_t in machining with the textured and conventional tools within the cutting velocity range from 120 to 360 m/min. The gaps of the cutting forces from the textured and conventional tools both tend to be narrowed with increasing of cutting velocity, indicating that the influence of derivative cutting on processing is gradually reduced in the wake of the increase of cutting velocity.

Since the plastic deformation of chip bottom is so intense that it is hard to prevent derivative cutting for the textures close to the cutting edge, the reducing of derivative cutting force is an alternative way to diminish its adverse effect on cutting performance of textured tools. As above analyses, the optimizing of the structural parameters of texture (reducing edge radius and inclined angle) helps minimize the effect of derivative cutting with increasing cutting velocity.

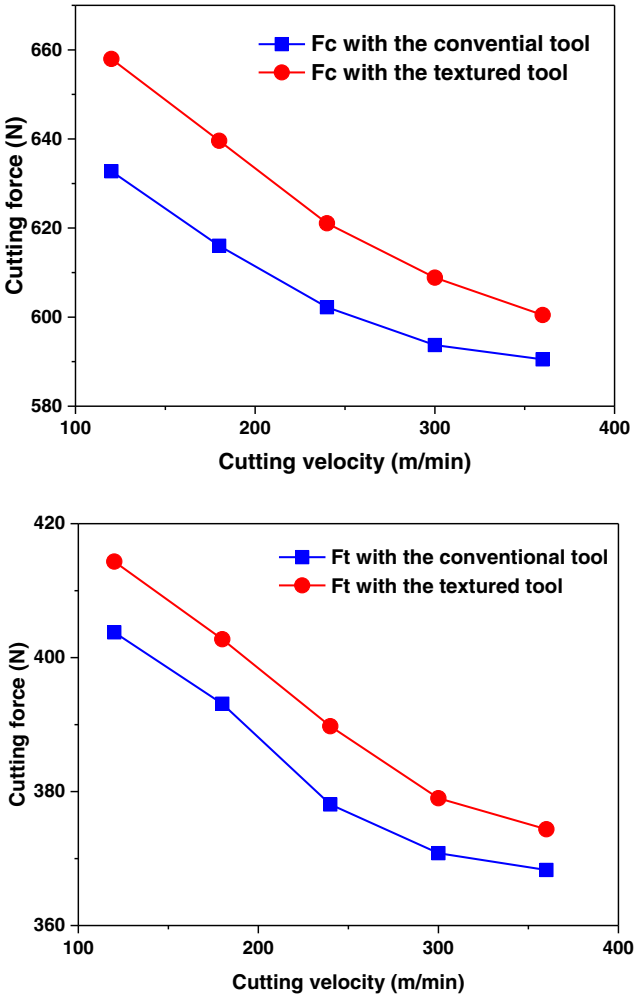

Fig. 17 The effect of cutting velocity on cutting forces under the constant conditions of the textures edge radius of 5 μm, the distance l_d of 150 μm, and the inclined angle of − 40°

6 Conclusions

A couple iteration model is build up to estimate derivative cutting force and tool force during the orthogonal machining. Derivative cutting force consists of derivative chip formation force and plowing force. The flow stress model for derivative cutting is combined with Oxley's cutting model to predict formation force of derivative chip. Meanwhile, Waldorf's slip-line model is applied to evaluate the plowing force in derivative cutting. Based on Oxley's prediction approach, the oblique moving band heat source theory is applied for modeling of cutting temperature, which is integrated with the derivative cutting model to build up the coupled iterative model. Finally, derivative cutting force and tool force are obtained via the cyclic iteration computations.

- A couple iteration model is build up to predict cutting force under effect of derivative cutting directly from the structural and positional parameters of textures, cutting conditions, and material properties without cutting test data, contributing to a better understanding of the mechanism of derivative cutting. The experimental validation shows that the proposed iteration model works well to predict cutting force.
- The proposed iteration model provides some ways to diminish the adverse effect of derivative cutting. Through analysis of the related prediction results, the optimizing of the structural parameters of texture (reducing edge radius and inclined angle) helps minimize derivative cutting force with increasing cutting velocity.

Funding information This work is supported by the National Natural Science Foundation of China (51675311) and Development Plan of Science and Technology of Shandong Province (2017GGX30115).

References

1. Xing Y, Deng J, Wang X (2016) Experimental assessment of laser textured cutting tools in dry cutting of aluminum alloys. J Manuf Sci Eng 138:071006
2. Kummel J, Braun D, Gibmeier J, Schneider J, Greiner C, Schulze V, Wanner A (2015) Study on micro texturing of uncoated cemented carbide cutting tools for wear improvement and built-up edge stabilization. J Mater Proc Technol 215:62–70
3. Zhang K, Deng J, Meng R, Lei S, Yu X (2016) Influence of laser substrate pretreatment on anti-adhesive wear properties of WC/Co-based TiAlN coatings against AISI 316 stainless steel. Int J Refract Met Hard Mater 57:101–114
4. Zhang K, Deng J, Xing Y, Li S, Gao H (2015) Effect of microscale texture on cutting performance of WC/Co-based TiAlN coated tools under different lubrication conditions. Appl Surf Sci 30: 107–118
5. Deng J, Wu Z, Lian Y, Qing T, Cheng J (2013) Performance of carbide tools with textured rake-face filled with solid lubricants in dry cutting processes. Int J Refract Metal Hard Mater 20:164–172
6. Deng J, Lian Y, Wu Z, Xing Y (2013) Performance of femtosecond laser-textured cutting tools deposited with WS_2 solid lubricant coatings. Surf Coat Technol 222:135–143
7. Sugihara T, Enomoto T (2009) Development of a cutting tool with a nano/micro-textured surface-improvement of anti-adhesive effect by considering the texture patterns. Precis Eng 33:425–429
8. Sugihara T, Enomoto T (2012) Improving anti-adhesion in aluminum alloy cutting by micro stripe texture. Precis Eng 36:229–237
9. Sugihara T, Enomoto T (2013) Crater and flank wear resistance of cutting tools having micro textured surfaces. Precis Eng 37:888–889
10. Ma J, Duong N, Lei S (2015) Numerical investigation of the performance of microbump textured cutting tool in dry machining of AISI 1045 steel. J Manuf Proc 19:194–204
11. Han W, Duong N, Ma J, Lei S (2017) CEL FEM investigation of effects of microgrooved cutting tools in high speed machining of AISI 1045 steel. ASME 2017 12th Int Manuf Sci Eng Conf
12. Han W, Ma J, Lei S (2018) FEM prediction of dislocation density and grain size evolution in high speed machining of Al6061-T6 alloy using microgrooved cutting tools. Int J Adv Manuf Technol 95:4211–4227
13. Duan R, Deng J, Ai X, Liu Y, Chen H (2017) Experimental assessment of derivative cutting of micro-textured tools in dry cutting of medium carbon steels. Int J Adv Manuf Technol 92:3531–3540
14. Duan R, Deng J, Ge D, Ai X, Liu Y, Meng R, Niu J, Wang G (2018) An approach to predict derivative-chip formation in derivative cutting of micro-textured tools. Int J Adv Manuf Technol 95:973–982
15. Oxley P (1989) Mechanics of machining, an analytical approach to assessing machinability. Ellis Horwood Limited, Chichester, England 123–150
16. Ozel T, Zeren E (2005) A methodology to determine work material flow stress and tool-chip interfacial friction properties by using analysis of machining. J Manuf Sci Eng 128:119–129
17. Johnson G R, Cook W (1983) A constitutive model and data for metals subjected to large strains, high strain rates and high temperatures. Proc 7th Int Symp 18:541–547
18. Li X (1997) Development of a predictive model for stress distributions at the tool-chip interface in machining. J Mater Proc Technol 63:169–174
19. Zorev N (1963) Inter-relationship between shear processes occurring along tool face and shear plane in metal cutting. International Research in Production Engineering ASME 42–49
20. Jaeger J (1942) Moving sources of heat and the temperatures at sliding contacts. J Proc R Soc 76:203–224
21. Hahn R (1951) On the temperature developed at the shear plane in the metal cutting process. Proc of First U.S. National Congress of Applied Mechanics. 661–666
22. Johnson W (1962) Some slip-line fields for swaging or expanding indenting, extruding and machining for tools with curved dies. Int J Mech Sci 4:323–347
23. Huang Y, Liang SY (2005) Cutting temperature modeling based on non-uniform heat intensity and partition ratio. Mach Sci Technol 9: 301–323
24. Fang N, Jawahir IS (2002) Analytical predictions and experimental validation of cutting force ratio, chip thickness, and chip back-flow angle in restricted contact machining using the universal slip-line model. Int J Mach Tools Manuf 42(6):681–694
25. Fang N, Jawahir IS, Oxley PLB (2001) A universal slip-line model with non-unique solutions for machining with curled chip formation and a restricted contact tool. Int J Mech Sci 43(2):557–580
26. Usui E, Hoshi K (1963) Slip-line fields in metal machining which involve centered fans. International Research for Production Engineering ASME 61:61–67
27. Jawahir I S (1986) An experimental and theoretical study of the effects of tool restricted contact on chip breaking, PhD Thesis, The University of New South Wales, Australia
28. Hills D A, Nowell D, Sackfield A (1993) Mechanics of elastic contacts. Butterworth Heinemann, London 32–40
29. Weber M, Hochrainer T, Gumbsch P, Autenrieth H, Delonnoy L, Schulze V (2007) Investigation of size-effects in machining with geometrically defined cutting edges. Mach Sci Technol 11:447–473
30. Joshi SS, Melkote SN (1998) An explanation for the size-effect in machining using strain gradient plasticity. JSME/ASME Int Conf On Materials and Processing pp:318–323
31. Waldorf DJ, Devor RE, Kapoor SG (1998) A slip-line field for ploughing during orthogonal cutting. J Manuf Sci Eng 120:693–699
32. Eleiche A, Campbell J (1976) Strain-rate effects during reverse torsional shear. Exp Mech 16(8):281–290
33. Devor R, Kapoor S (2004) On the modeling and analysis of machining performance in micro-endmilling, part I: surface generation. J Manuf Sci Eng 126:685–694